

The influence of nucleation on cavitation inception in tip-leakage flows

P. S. Russell, L. Barbaca, J. A. Venning, B. W. Pearce & P. A. Brandner
(Australian Maritime College, University of Tasmania, Australia)

ABSTRACT

Cavitation in tip leakage flow for a stationary hydrofoil analogy is investigated experimentally in a cavitation tunnel. Details of the hydrofoil design process, including the development of rigorous mathematical tools for definition of hydrofoil section geometries and fairing of the tip to suppress flow separation in the gap, are discussed. The experiments were performed for different tip clearances (τ) and hydrofoil incidences (α), but for a fixed chord based Reynolds number of 3×10^6 . The influence of nucleation on cavitation inception is evaluated by performing tests with a natural nuclei population and an abundantly seeded population of large nuclei. Cavitation was characterized using high-speed imaging and acoustic measurements. The hydrofoil design was shown suitable for studying tip leakage flow cavitation, addressing the issues reported in the previous work. Following an initial survey of developed cavitation topology for a range τ and α values, $\alpha = 6^\circ$ was selected for more detailed study of cavitation inception. From the acoustic measurements a critical gap height, with the worst performance in terms of cavitation inception, was established at $\tau = 0.8$ for natural nuclei flow. For the abundantly seeded flow cavitation was present for the highest cavitation number achievable in the experimental facility across the complete range of τ values and inception could not have been characterized. Acoustic measurements reveal cavitation to be generally intermittent for natural nuclei flow, becoming continuous as seeding is introduced. While a continuous cavity in the seeded flow resulted with a higher baseline acoustic signature, cavity collapse observed during merging of subsequent events in the natural nuclei flow was observed to be a feature generating the highest instantaneous peaks in the acoustic pressure.

INTRODUCTION

Tip-Leakage Flow (TLF), i.e. the flow in the gap between the tip of a rotating blade and a static casing, is a feature observed in many fluid mechanics applications, most prominently in axial turbomachinery and ducted propulsors. Due to the complexity of the flow through the gap and a high blade-tip velocity, TLF is often a flow feature with the global pressure minimum, and consequently highest susceptibility to cavitation inception.

Cavitation in tip leakage flows can occur in many forms, but for a well designed gap geometry, cavitation inception is most likely in the tip-leakage vortex (TLV). However, experimental studies using a rotating model, particularly at large Reynolds number, report cavitation inception in the small vortical filaments originating from the tip trailing edge (Oweis & Ceccio, 2005) and the jetting shear layer on the suction side of the hydrofoil (Wu *et al.*, 2011).

While the mean pressure in the cores of the vortical filaments is higher than that in the core of a nominally stronger TLV, interactions between the weaker filaments and the TLV can lead to the filament stretching and a sudden instantaneous drop in the filament core pressure. Consequently, instantaneous pressure in the core of the filaments can decrease below that in the core of the TLV, making the vortical filaments sites of the global pressure minimum and cavitation inception (Oweis & Ceccio, 2005; Chang *et al.*, 2012). This transient type of small-scale cavitation inception has been documented in axisymmetric jets (Gopalan *et al.*, 1999; Ran & Katz, 1994) as well as in plane shear layers (O'Hern, 1990) or behind a backward-facing step (Agarwal *et al.*, 2020; Barbaca *et al.*, 2020b).

TLF is characterized by a multitude of in-

tracting flow features which affect the inception of cavitation. Unbounded finite-span lifting surfaces generate trailing vortices due to spanwise flows near the tip driven by the pressure difference between the two sides of the hydrofoil. This reduces the lift generated in the vicinity of the tip, increases the drag of the wing and provides a mechanism for the downstream transport of vorticity from the hydrofoil surface. The cores of these trailing vortices are characterised by high rotation rates and low pressures. As confinement is introduced in the vicinity of the tip, and flow through the gap reduces, the pressure difference between the sides of the hydrofoil increases. For small clearances, the leakage flow is suppressed, producing a more two-dimensional flow, higher lift, and a weaker trailing vortex. However, the difference in pressure increases the angle between and flow through the gap and free-stream flow which may induce local separation at the trailing edge. It may also induce development of low-pressure areas at the leading edge and flow separation within the gap which promote cavitation. Rounding of the edge on the pressure side of the hydrofoil tip can be utilized to mitigate flow separation and cavitation within the gap, however, it is often accompanied by increased shear on the foil suction side contributing vorticity to the TLV (Laborde *et al.*, 1997).

Treatments to the pump or duct casing, such as circumferential grooves, have been applied in an effort to mitigate cavitation, but must be implemented with care as these regions can act as sites for re-nucleation of cavitation once incepted, and tend to be ineffective at larger gap clearances (Dreyer, 2015). Likewise, modification of the tip geometry such as tip extensions and other tip treatments can offer benefits but their effectiveness varies greatly with the gap clearance (Cheng *et al.*, 2021).

In order to reduce modelling complexity, single stationary hydrofoil analogies of multi-bladed rotating geometries have been explored both experimentally (Boulon *et al.*, 1999; Gopalan *et al.*, 2002; Higashi *et al.*, 2002; Dreyer, 2015; Russell *et al.*, 2020a) and numerically (You *et al.*, 2006, 2007; Zhang *et al.*, 2015; Guo *et al.*, 2016). Although, many aspects of the flow are not captured with a single hydrofoil analogy, these approxima-

tions have proved to be a useful tool in exploring a number of flow features that are also observed experimentally in the rotating flows they emulate.

An aspect of the TLF that to date has not been appropriately addressed is the effect of the water nuclei content on cavitation. In order for cavitation inception to occur, the water must contain sites of weakness, also termed ‘nuclei’, which are typically found in the form of microbubbles. It has been shown that nuclei content has a significant effect on cavitation inception and the dynamics of developed cavitation in model testing (Boulon *et al.*, 1997; de Graaf *et al.*, 2016; Venning *et al.*, 2017; Khoo *et al.*, 2021) and, therefore, a capability to precisely control the water nuclei content is mandatory in hydrodynamic facilities for studying cavitation.

Gopalan *et al.* (2002) studied the effect of seeding the TLF with nuclei generated via electrolysis and observed a fiftyfold increase in the cavitation event rate between the seeded and unseeded flow for the same cavitation number. However, their observations might have been exaggerated by relatively large size of the nuclei in comparison to the model. Russell *et al.* (2020a,c) recently reported studies of TLF cavitation for a hydrofoil model with a square-edged tip for a flow with the natural nuclei (deplete) content and a flow artificially seeded with an abundant polydisperse nuclei population. They note that the topology and acoustic signature of developed cavitation remain similar for the two nuclei populations. However, differences in desinent behaviour were observed, where for the nuclei deplete flow desinence is sudden and for nuclei abundant flow it is more gradual.

The effect of nuclei on cavitation inception has been investigated in more detail for a three-dimensional hydrofoil in an unbounded flow. In this case, the most likely site of cavitation inception is within the low pressure core of the vortex trailing from the hydrofoil tip and this phenomena is referred to as tip vortex cavitation (TVC). Earlier experimental studies on the effect of nuclei on the TVC inception were performed by indirectly controlling the nuclei content via the water dissolved gas content (Arndt & Maines, 1994; Chang *et al.*, 2012) or via microbubble injection into the

test flow (Briancon-Marjollet & Merle, 1996; Peng *et al.*, 2017). Recently, Khoo *et al.* (2021) reported a study of TVC inception for the natural and two types of seeded nuclei populations (polydisperse and monodisperse). They describe the effect of nuclei concentration and size distribution on the location of the inception within the vortex core and the flow acoustic signature. Nuclei size was observed not only to influence inception due to the size-dependent critical pressure, but also by affecting the physics of nuclei capture by the vortex.

Previous studies of TLF at the Australian Maritime College (AMC) Cavitation Research Laboratory (CRL), performed using a NACA 0012 hydrofoil model equipped with interchangeable square-edge tips, revealed issues with premature cavitation in the gap, local sources of nucleation at the discontinuity between the tip and the hydrofoil main body and sheet cavitation at the hydrofoil base due to the use of a thicker NACA 0040 foil section to prevent model vibration (Russell *et al.*, 2020*a,c*). In order to alleviate these issues, a new hydrofoil model with a custom-designed cambered section and a complex tip rounding, has been designed for the present work. The hydrofoil section is also optimised for the maximum ratio of the lift to the negative local pressure. A new experimental apparatus has been developed enabling continuous adjustment of the hydrofoil incidence and the tip clearance.

Cavitation inception for the optimised hydrofoil will be explored using rigorous modelling of different free-stream nuclei populations. For the current work, these include the natural nuclei population and an abundant polydisperse population of comparatively large nuclei. These populations represent the two extremes in which turbomachinery and ducted propulsors normally operate and highlight the differences in the cavitation inception dynamics induced by variation of the water nuclei content.

HYDROFOIL SECTION DESIGN TOOLS

Initial iteration of the hydrofoil section design was based on standard NACA thickness profiles and the ‘roof-top’ camber lines of the NACA

a series. Without computing the conformal mapping used to derive these sections, profiles are generally defined with a set of ordinate pairs, which are interpolated to form a continuous section profile once camber has been applied (Abbott & von Doenhoff, 1959). However, interpolation can lead to piece-wise continuous, but non-smooth variations in curvature.

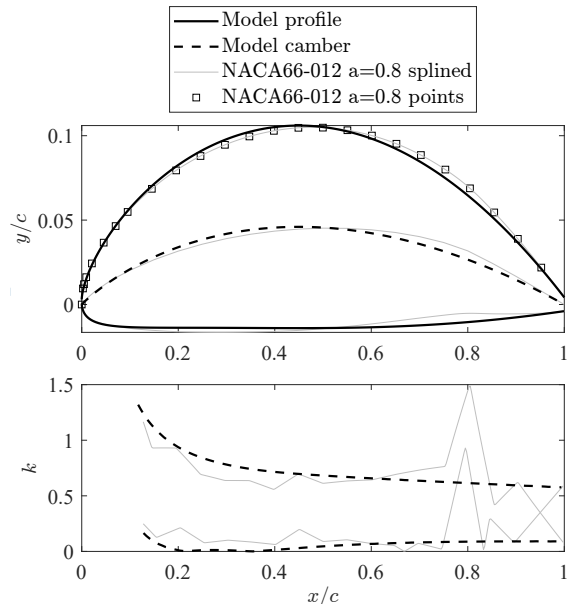


Figure 1. a) A splined NACA 66-012 (mod), $a = 0.8$ profile from discrete points is compared to the tip section geometry used in the experiment. b) Curvature of the splined profile is piece-wise continuous but non-smooth.

An example of this effect is plotted for a NACA 66-012 thickness distribution with a NACA $a = 0.8$ camber profile using a simple cubic spline interpolation in figure 1. While these variations are small and generally below the manufacturing tolerances for larger blades—such as those on ships—at model scale and in numerical simulations they can induce flow perturbations. More complex interpolation schemes using equivalent ellipses with a correction to ensure a defined leading edge radius can be applied to circumvent the issue (Carlton, 2007). However, these additional methods render the reproduction of section profiles into a convoluted process.

To simplify profile geometry generation and ensure a smooth variation of the profile curva-

ture, mathematically rigorous tools for definition of the thickness distribution and camber profile have been developed. The developed tools are capable of producing geometries similar to the classic NACA profiles.

The resulting equations encapsulate the key hydrodynamic parameters into the profile definition such that the geometry is meaningfully specified. The profile thickness distribution can be fully specified by prescribing: the leading edge radius (r_{LE}), the maximum profile thickness (y_{max}), the chordwise location of maximum thickness (x_{max}) and the profile thickness at the trailing edge (y_{TE}). The profile is split into two regions defined by the following equations

$$y(x) = a_0 x^{1/2} + a_1 x^1 + a_2 x^2 + a_3 x^3, \quad (1)$$

$$x \leq x_{max}$$

$$y(x) = b_0 + b_1 x^1 + b_2 x^2 + b_3 x^3 + b_4 x^4, \quad (2)$$

$$x \geq x_{max}$$

For very small x values, the polynomial terms in 1 are negligible, with the remaining square root term defining a nearly elliptic profile such that the leading edge radius is approximately $r_{LE} \approx 2a_0^2$ (Pearce,). The other coefficients are solved by specifying the location of maximum thickness, for which the first and the third derivative are zero to ensure a smooth curvature.

$$y(x) = \begin{cases} a_0 & = \sqrt{0.5 r_{LE}} \\ y(x_{max}) & = y_{max} \\ y'(x_{max}) & = 0 \\ y'''(x_{max}) & = 0 \end{cases} \quad (3)$$

The coefficients for the trailing portion, b_n , are specified from the end points, and by asserting that derivatives match with the incoming derivatives from the leading edge portion of the curve.

$$y(x) = \begin{cases} y(1) & = y_{TE} \\ y(x_{max}) & = y_{max} \\ y'(x_{max}) & = 0 \\ y''(x_{max} - \epsilon) & = y''(x_{max} + \epsilon) \\ y'''(x_{max}) & = 0 \end{cases} \quad (4)$$

These details are presented graphically in figure 2 alongside the ordinates of a NACA66 (mod) section for a comparison (Brockett, 1966). Favourable agreement is found between the two profiles, however, the developed mathematical definition provides a convenient expression for the thickness at any point along the section chord.

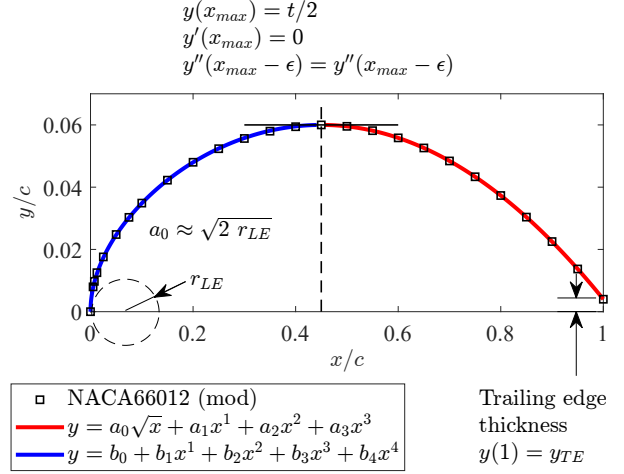


Figure 2. A solution for the definition of the thickness profile is plotted. Annotated are the equations, main parameters, and boundary condition that influence the shape of the profile. The sample section closely approximates reference points for a NACA 66-012 (mod) thickness form.

In a similar manner to the profile thickness distribution, a mathematically rigorous definition of the camber curve has been developed. The constraining parameters were selected based on the flow features, ensuring simple yet flexible definition of the curve, which preserves smooth variation of the curvature required to produce a faired geometry.

The classical logarithmic camber curve with its uniform loading does produce such a curve (Breslin & Andersen, 1994), but as discussed by Kerwin & Hadler (2010) can produce geometries that are too “greedy” and susceptible to flow separation. This motivated generation of the NACA a -series ‘roof top’ camber curves (Abbott & von Doenhoff, 1959). These curves have a rather sharp transition at the intersection of the uniformly loaded region extending from the leading edge and the region characterised by a linear reduction in loading towards the trailing edge. Not only does this lead to a spike in curvature as seen in figure 1, but also it predisposes the geometry to a cusped trailing edge.

To produce a smooth variation of the first three derivatives, and thus curvature, a cubic Bézier formulation of the camber curve was employed. Cubic Bézier curves are formed from four points P_n , $n \in [0, 1, 2, 3]$, with the end points fixed in chord normalised ordinates at the origin ($P_0 = (0, 0)$) and $P_3 = (0, 1)$. Normalised ordinates then follow the parameterised matrix equation

$$\begin{bmatrix} x \\ y \end{bmatrix} (t) = \sum_{i=0}^3 \binom{3}{i} (1-t)^{3-i} t^i \mathbf{P}_i, \quad (5)$$

where $t \in [0, 1]$.

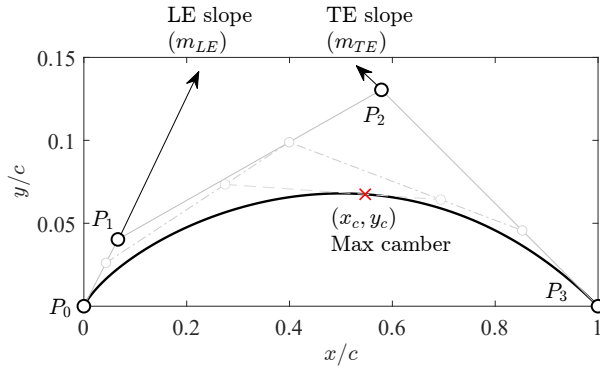


Figure 3. A graphical representation of De Casteljau’s algorithm used to outline the production of infinitely differentiable camber curves using a cubic Bézier formulation. The curves are based on three parameters, the slope of the camber curve at the leading edge (m_{LE}), the trailing edge (m_{TE}), and the location of maximum camber (x_c, y_c).

The two middle points, P_1 and P_2 , are constrained to lie along the lines corresponding to an idealised incoming and exiting flow direction if the camber curve acted as a zero-thickness turning vane (figure 3). Although the flow streamlines are dependent on the profile thickness distribution and the incidence, this represents a thin plate equivalent satisfying the requirement of a shockless entry and the Kutta condition about the hydrofoil. These two lines define the slopes of the section leading (m_{LE}) and trailing (m_{TE}) edges. To uniquely define the locations of P_1 and P_2 along these lines and to allow for those to be resolved explicitly, the location of the maximum camber must be specified. Depending on the location of maximum camber (x_c, y_c) the distance between the $P_{1,2}$ and the curve endpoints can become very short, and in cases where the location

of the maximum camber falls too close to the projected leading and trailing edge slopes, no solution is found. For moderate camber specification, where $0.3 \leq x_c \leq 0.7$ this is not a problem. As with the NACA camber profiles, the curve offset can be scaled in the y direction, noting that this results with an increase in the leading and trailing edge slopes.

The method presented for camber specification can be used to generate curves similar to the NACA series, with the benefit of a smooth transition between regions (figure 4). The described tools for mathematical definition of both the section thickness distribution and the camber, are used to develop the section geometry of the experimental hydrofoil model.

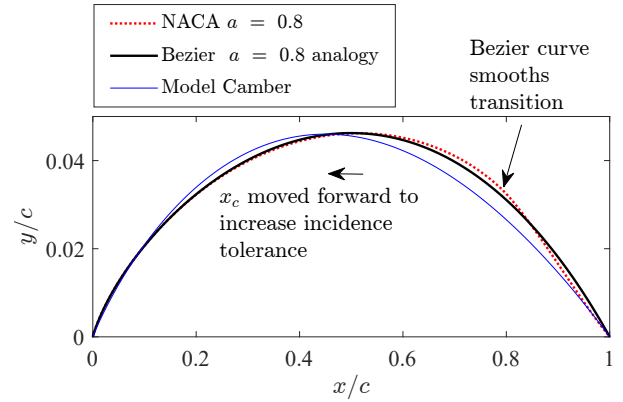


Figure 4. Bézier camber curves defined using the method developed are compared to a reference NACA ‘rooftop’ camber curve. The Bézier camber curve eventually used for the model tip section profile is also plotted.

HYDROFOIL GEOMETRY DESIGN

For a stationary hydrofoil analogy to faithfully emulate the flow features of a high Reynolds number rotating TLF, distribution of sectional profiles along the hydrofoil model span has to be carefully considered. A particular difference, with regards to cavitation inception, stems from an increase in circumferential velocity from the root towards the tip of a rotating blade. Due to the circumferential velocity distribution, the tip region of a rotating blade is the most likely site of cavitation inception.

In contrast, a stationary hydrofoil model experiences a uniform inflow, which can lead to cav-

itation forming at the hydrofoil root. This problem is compounded by the requirements for low model vibration and tip deflection, which in prior experiments at the AMC (Russell *et al.*, 2020a,c), were addressed via increasing the thickness of the hydrofoil model root section. The added thickness resulted in a decrease in the minimum pressure about the root section and for some conditions the root was found to be the site of global cavitation inception. This had a detrimental effect on the acoustic characterization of the TLF cavitation, as the noise generated by collapse and condensation of the cavity forming at the root obscured the acoustic signature of cavitation inception in the TLV (Russell *et al.*, 2020a).

A potential solution for this issue is to twist the model, i.e. reduce the incidence of the root section, however, a resulting complex three-dimensional geometry would require time consuming optimisation using Computational Fluid Dynamics modelling. Instead, for the current work it was elected to maintain the pressure distribution on the suction side by balancing the increase in the section thickness with a decrease in the section camber.

Based on these considerations, a hydrofoil model geometry with sectional profiles designed using the above described mathematical tools for section definition and evaluated using XFOil two-dimensional numerical code (Drela, 1989) has been developed. The model is designed with a constant section profile maintained from the tip for a third of the span. The section profile varies across the remainder of the span, with the section thickness increasing linearly towards the root to ensure adequate stiffness of the model. The section profiles at various locations along the span are presented in figure 5.

Common to many previous studies of the TLF is the use of hydrofoil models with symmetric sections (Dreyer, 2015; Russell *et al.*, 2020a,c). The topology of the TLF observed in these studies was characterized by a well defined TLV, but lacking secondary vortical structures typically observed in the experiments with a rotating model (Oweis & Ceccio, 2005; Wu *et al.*, 2011). The lack of secondary structures can be attributed to the low lift generated by symmetric sections and consequent

less intense flow through the gap. An obvious solution to this issue is to increase the section incidence (α). However, due to the low ratio of the lift coefficient (C_L) and the minimum pressure coefficient on the foil suction side (C_p), an increase in α results with onset of cavitation on the foil face detrimental to characterization of the inception in the TLF. An alternative method to increase the section lift is to apply camber.

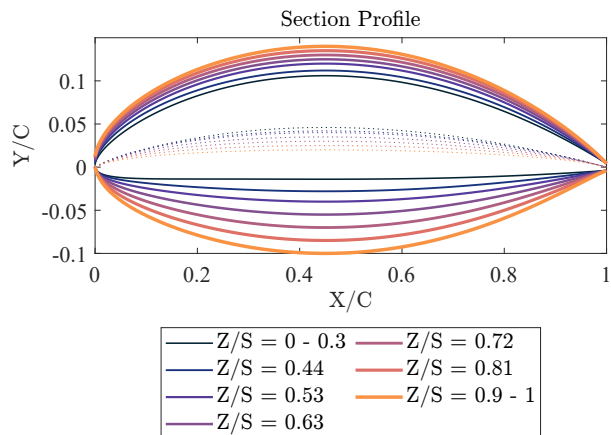


Figure 5. Section profiles used to generate the hydrofoil model are presented. The spanwise location of profile section z have been normalised by the overall span of the hydrofoil s . Note the differences in scale between the axes.

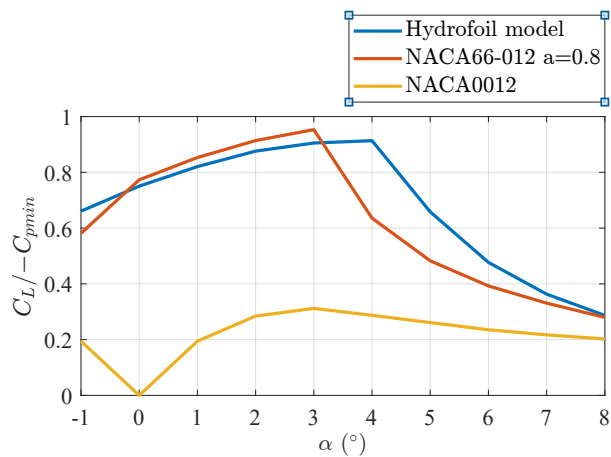


Figure 6. Sectional lift normalised by the incurred minimum pressure coefficient is plotted for a range of incidence angles.

With consideration to cavitation performance and to match the common propulsor geometries studied in the literature, a section with the thickness distribution analogous to a NACA66-012 mod profile and a Bèzier curve representation of a

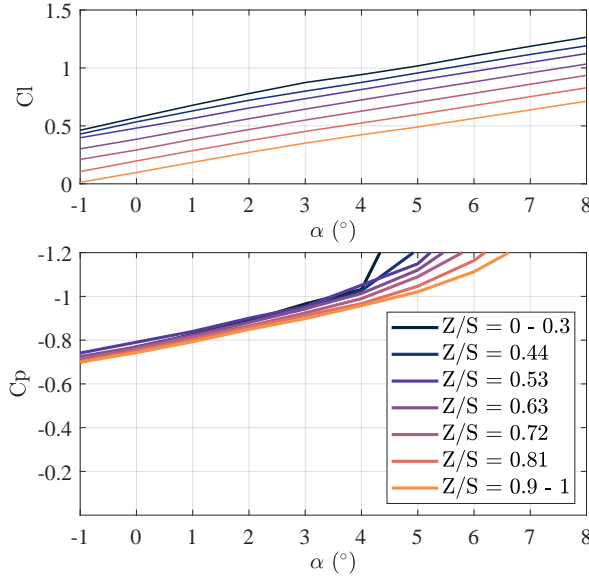


Figure 7. Lift and minimum pressure coefficient are plotted for each section profile along the span of the hydrofoil.

NACA $a = 0.8$ camber line was chosen for the tip section of the hydrofoil (figure 5). Cavitation performance was evaluated using the ratio of the sectional C_L and the negative of the minimum C_p , with the selected section geometry representing a trifold improvement over a NACA0012 section used in the original AMC work (figure 6).

In applied situations, such as in the wake of a ship, the inflow to the hydrofoil is often turbulent, requiring the section geometry to have a good tolerance to variation in incidence. To achieve this, the location of maximum camber of the selected section was moved forward from $x/c = 0.5$ to $x/c = 0.45$, helping suppress the development of a low-pressure peak at the leading edge. This modification results with a reduction in maximum $C_L / -C_p$ (figure 6), however, the gain in the incidence tolerance exceeds the importance of the small loss in cavitation performance for optimum α . An additional benefit originating from this change in the sectional geometry is a delayed flow separation, which can be attributed to a reduction in loading towards the trailing edge.

As per previous discussion, from the hydrofoil section was varied from the location a third of the span from the tip towards the root. The section profiles are chosen to maintain a similar sectional lift, which was achieved for all but the sections clos-

est to the root. For these, in order to ensure that minimum in the pressure coefficient remains within the acceptable range, the lift was allowed to decrease. Sectional geometries at selected locations along the hydrofoil span are presented in figure 5, while the dependence of their respective C_L and C_p for a range of α values is presented in figure 7.

In prior work by Russell *et al.* (2020a,c), it was observed that a flow separation at the sharp edge on the pressure side of the tip induces early onset of cavitation within the gap. Gap cavitation generates a cloud of bubbles that nucleate the TLV. To suppress the flow separation and delay the onset of the gap cavitation, a complex fairing is applied to the tip of the hydrofoil. On the pressure side, a radius equal to a quarter of the section thickness is applied from $x/c = 0.2$ to $x/c = 0.8$. From $x/c = 0.8$ to the trailing edge, the radius is varied and is equal to the half of the section thickness at the respective x/c coordinate. A constant 1 mm radius is applied to the suction side edge from $x/c = 0.2$ to the trailing edge. The nose section of the tip, i.e. $0 \leq x/c \leq 0.2$, is a complex lofted surface generated by blending the pressure and suction side radii with the section leading edge profile. The details of the tip rounding are schematically represented in figure 8.

EXPERIMENTAL SETUP

The experiments were performed in the University of Tasmania variable pressure water tunnel. The tunnel test-section is 0.6×0.6 m square at the entrance, by 2.6 m long. The test-section ceiling is horizontal with the floor sloping 20 mm over the length to maintain nominally constant speed and a zero-stream-wise pressure gradient. The operating velocity and pressure are controlled independently, with ranges from 2 to 13 m/s and 4 to 400 kPa absolute, respectively. The tunnel volume is 365 m^3 and is filled with demineralised water. Optical access is provided through acrylic windows on each side of the test-section.

The test-section absolute pressure is measured, depending on the value, from high- or low-range Siemens Sitrans P absolute pressure transducers models 7MF4333-1FA02-2AB1 (range 0–

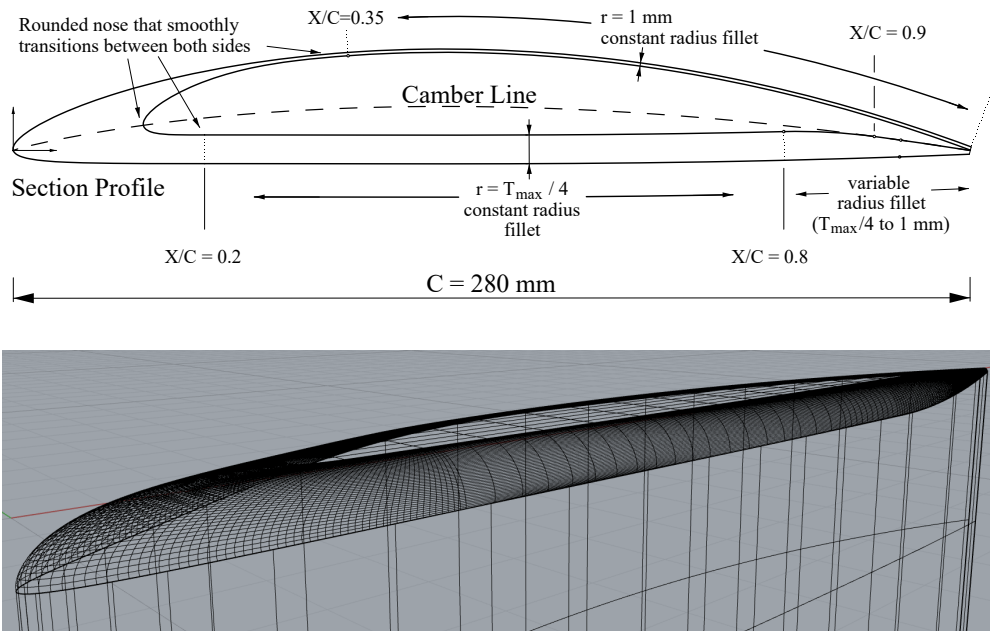


Figure 8. Schematic of the fairing applied to the tip geometry of the hydrofoil to minimise flow separation and cavitation within the gap. A 3D representation of the hydrofoil tip is shown below.

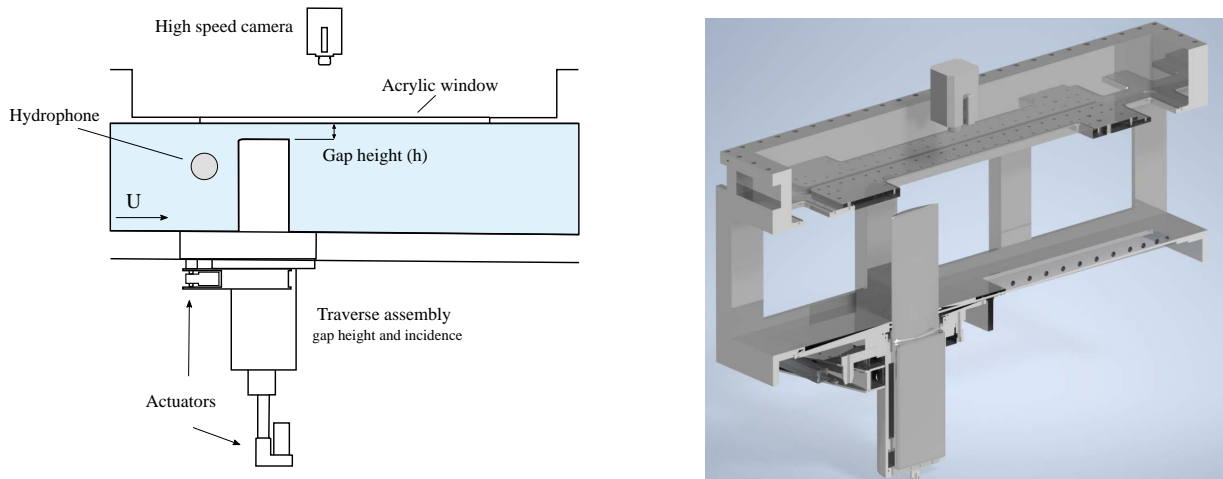


Figure 9. A schematic of the hydrofoil model mounted in the tunnel test section via a traverse assembly. A 3D model of the tunnel test-section, the hydrofoil and the traverse assembly is shown in the image on the right.

130 kPa) and 7MF4333-1GA02-2AB1 (range 0–400 kPa), with estimated precisions of 0.13 and 0.48 kPa respectively. The test-section velocity is measured from the calibrated contraction differential pressure. Depending on the value, either low- or high-range Siemens Sitrans P differential pressure transducers models 7MF4333-1DA02-2AB1-Z (range 0–25 kPa) and 7MF4333-1FA02-2AB1-Z (range 0–160 kPa) are used, with estimated precision of 0.007 and 0.018 m/s respectively. The test section velocity has been measured to be spatially uniform to within 0.5%, has a temporal variation of less than 0.2%, and a free stream turbulence intensity of 0.5%. The water dissolved gas content is measured using an Endress+Hauser Oxy-Max WCOS 41 membrane sensor. Further details on the facility can be found in Brandner *et al.* (2006, 2007).

The experimental setup has been developed to study cavitation in the gap flow between a stationary hydrofoil and the ceiling of the tunnel test-section, as schematically represented in figure 9. The hydrofoil and mounting block are made out of a single forged stainless steel billet. The hydrofoil has a chord of $c = 280$ mm, and the span can be varied between $s = 540$ mm and 610 mm. The use of a NACA 66-012 mod section analogy at the tip, results with a tip thickness, $t = 33.6$ mm. The hydrofoil tapers towards the root, with the maximum root thickness of 67.2 mm. A 90 mm long parallel section is added between the hydrofoil root and the mounting block to ensure a streamlined flow along the foil/wall junction as the foil is traversed in the vertical direction. The mounting block is a 290 mm long \times 100 mm wide \times 605 mm high prism housed within the traversing assembly. The traversing assembly allows for a continuous adjustment of the tip gap (h) and the incidence (α) of the hydrofoil. For the present work the gap could be adjusted in the range $1 \leq h \leq 70$ mm and the incidence in the range $-10^\circ \leq \alpha \leq 10^\circ$. The gap and the incidence adjustments were controlled using Tolomatic 32RSA-HT1 stepper motor electric linear actuators, driven by a Tolomatic ACS stepper driver motor controller, with a maximum thrust of 18.5 kN. The actuators have an accuracy of 0.01 mm across a 300 mm travel. The hydrofoil lead-

ing edge is located ≈ 900 mm downstream of the test-section entrance with the unperturbed incoming wall boundary layer thickness at that position being $\delta = 19$ mm.

High-speed imaging of the cavitation topology in the gap was acquired using a Phantom v2640 camera with a maximum resolution of 2048×1952 pixels, mounted above the tunnel test section. The camera was equipped with a Nikon AF Nikkor 24 mm f/2.8 D lens with the images acquired at a cropped resolution of 2048×640 pixels at a sampling rate of 10000 frames per second. Continuous illumination was provided from two Effilux EFFI-BL-LITE-1M12P 650×650 mm LED panels mounted to the side of the test section and three Veritas Constellation 120 LED lamps mounted above and to the side of the test section. The image acquisition was controlled via Phantom PCC 3.4.4 software. Optical access to the gap was provided through a 1150 mm long \times 215 wide acrylic window in the test section ceiling.

Acoustic measurements were obtained using a Brüel & Kjær Type 8103 hydrophone (voltage sensitivity $25.1 \mu\text{V}/\text{Pa}$) mounted in a flooded cavity (kept at the same pressure as the tunnel test section) beneath a 10 mm polyurethane diaphragm, with a 149 mm sensing diameter (Doolan *et al.*, 2013). The hydrophone was mounted in the side wall, 150 mm below the ceiling and approximately a chord length upstream of the hydrofoil leading edge. The signal was conditioned using a Brüel & Kjær Nexus conditioner and amplifier, which was also used to apply a 0.1 Hz - 100 kHz bandpass filter. The filtered signal was acquired using a National Instruments PXIe-4497 card at a sampling rate of 204.8 kS/s. Each acoustic measurement was performed for a period of 60 s.

The high-speed imaging and the acoustic measurements were triggered independently, however, the data was synchronized by recording the camera trigger signal along with the acoustics and using it to align the two datasets. The camera was operated with a post trigger, so that once an incipient event was manually observed or heard, the camera trigger could be activated.

The experiments were performed for the

hydrofoil chord-based Reynolds number, $Re = Uc/\nu = 3 \times 10^6$, where U is the mean flow velocity and ν is the water kinematic viscosity. The cavitation number is defined as $\sigma = (p - p_v)/0.5\rho U^2$, where p is the static pressure at the tunnel ceiling, p_v is the water vapour pressure and ρ is the water density. The hydrofoil clearance was non-dimensionalised by the maximum thickness of the hydrofoil tip section, $\tau = h/t$.

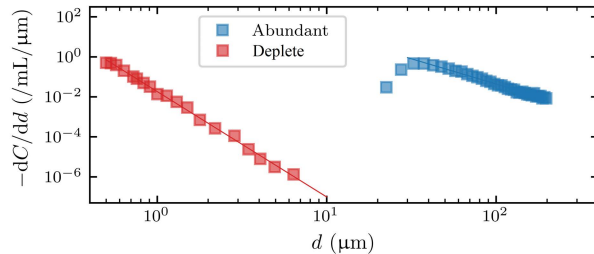


Figure 10. Cumulative size distribution of the natural and abundant polydisperse populations used for characterization of the effect of nuclei on the TLF.

The experiments were performed for a tunnel natural nuclei population and for an abundant polydisperse population generated via artificial seeding of the tunnel water with microbubbles. The tunnel natural nuclei population was characterized by Khoo *et al.* (2020) using measurements acquired via mechanical activation in a Cavitation Susceptibility Meter (CSM). Khoo *et al.* (2020) demonstrated that this population is practically invariant to tunnel operating conditions for dissolved oxygen levels below 4 ppm. Current experiments were performed with a dissolved O_2 content between 2.75 and 3.5 ppm.

Microbubbles for artificial nuclei seeding are generated via rapid depressurization of supersaturated water through an orifice, with a device referred to as ‘mini-tube’ (Barbaca *et al.*, 2020a). An array of 10 mini-tube devices was utilized to generate a nuclei plume seeding the top third of the test section and 50 mm each side of the tunnel centre line. Each device produces microbubbles at a rate of $\approx 10^6$ Hz. The resulting nuclei population in the test-section was characterized by Russell *et al.* (2020b) using Mie-Scattering Imaging (MSI). Cumulative size distributions for the both, natural and abundant, nuclei populations are given in figure 10.

RESULTS AND DISCUSSION

Developed Cavitation Topology

To perform an initial survey of the TLF topology across a range of α and τ values for both nuclei populations, high-speed imaging of developed cavitation ($\sigma = 1.35$) was utilized. Extracted frames from the high-speed recordings obtained at various conditions are presented in figures 11 & 12.

For the natural nuclei population, with the hydrofoil at zero incidence to the flow, thin intermittent incipient structures are observed in the TLV downstream of the foil. These structures rapidly grow from the initial size of the nucleus to form a short cavity that is simultaneously transported downstream. The location of inception has a stochastic character, from visual observation of high-speed data, this appears to shift downstream with an increase in τ .

With the introduction of nuclei, the cavitation in the TLV becomes less intermittent and the inception location moves closer to the hydrofoil. This can be attributed to a high availability of larger nuclei with the critical pressure close to p_v incepting almost instantly as they reach the low-pressure core of the TLV and continuously merging into the main cavity volume. Similarly to the flow with the natural nuclei, the cavity leading edge shifts downstream along the hydrofoil chord with an increase in τ . This phenomena is more easily observed in the seeded flow due to less intermittent nature of cavitation. In addition, the deviation in the vortex trajectory, characteristic of the TVC in an unbounded flow, also becomes increasingly prominent with larger clearances.

For $\alpha = 3^\circ$ similar trends were observed. The TLV becomes more deflected from the hydrofoil due to an incidence-induced increase in the flow through the gap. Generally, the cavities are thicker than those observed for $\alpha = 0^\circ$, reflecting the increase in the diameter of the core of the TLV with increase in α and related increase in lift. For the flow with natural nuclei populations, incipient events become less intermittent than at $\alpha = 0^\circ$, with subsequent events occasionally incepting before the prior events are washed away. In such instances,

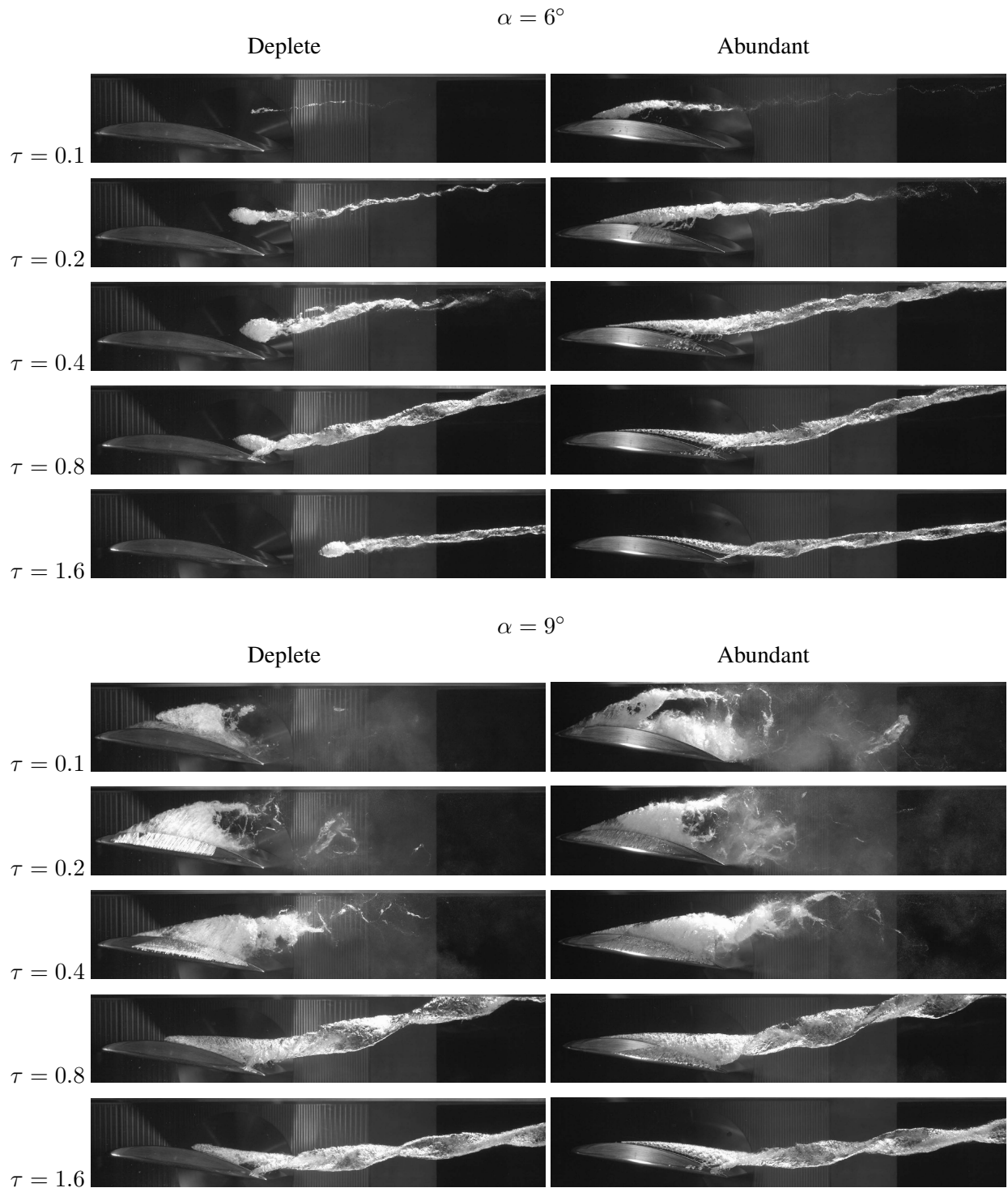


Figure 12. Developed cavitation topology at $\alpha = 6$ & 9° , $Re = 3 \times 10^6$, and $\sigma = 1.35$, for both the natural and abundant population of free-stream nuclei.

the new incipient event grows rapidly along the TLV and merges with the prior cavity downstream. This merging is characterized by a spike in the acoustic signature and will be further discussed in the next section.

For the low α values, the TLV is strong compared to the other sources of vorticity so it remains well defined and with little oscillations in its trajectory. With an increase in incidence to $\alpha = 6^\circ$, the topology of the TLV becomes more complex with the flow through the gap beginning to noticeably alter the trajectory of the TLV. For the large τ values, the cavity is deformed into a twisted helical ribbon resulting from the merger of the TLV and the vortex originating from the tip trailing edge. The helical merger of these vortices indicates their co-rotating orientation.

For the seeded flow at $\alpha = 6^\circ$, travelling bubble and sheet cavitation were observed within the gap. Cavitation within the gap nucleates braids of shed vorticity, associated with a jetting shear layer on the suction side of the tip, which bridge the gap and TLV cavities. These braids indicate the presence of sources of secondary vorticity, often postulated as the sites of cavitation inception in the TLF due to the large instantaneous variations in the pressure (Oweis & Ceccio, 2005; Wu *et al.*, 2011). However, the inception for seeded flow at high α values was not sufficiently resolved to ascertain whether these are indeed the sites of cavitation inception. This will be the subject of future work.

Limited cavitation within the gap for flow with the natural nuclei population, even though cavitation was well developed, shows a marked improvement over the geometry previously tested (Russell *et al.*, 2020a,c). Where cavitation in the gap was present, it was mainly associated with the small edge radius on the pressure-side due to the limitations imposed by a decrease in the section thickness towards the tip trailing edge. Cavitation in the gap for small τ values is suppressed due to reduced flow through the gap and an increase in distance between the TLV trajectory and the tip trailing edge. The trend of increased separation of the TLV from the hydrofoil trailing edge with decrease in τ is maintained across the range of tested α . As discussed in detail by Boulon *et al.* (1999), this is

largely an inviscid phenomena stemming from the proximity of the wall, which implies an image vortex which induces a larger incidence of the flow through the gap, migrating the TLV away from the tip.

Further increase in the incidence to $\alpha = 9^\circ$, resulted in further increase in the intensity of the tip trailing edge vortex for large τ values. For $\tau \leq 0.4$, a greater proportion of the lift is maintained at the tip, so that for $\alpha = 9^\circ$ cavitation on the hydrofoil face was observed. A further increase in the incidence of the flow through the gap, coupled with the instabilities from the collapse of cloud cavities now forming on the hydrofoil face, induced the TLV to bursting and complete disintegration with a decrease in τ .

From these observations of the developed cavitation topology, an incidence of $\alpha = 6^\circ$ was selected for further investigation of cavitation inception for a range of conditions outlined in table 1.

Flow Conditions

Re	3×10^6						
α	6°						
τ	0.1	0.2	0.4	0.6	0.8	1	
		1.2	1.4	1.6	1.8	2	
σ	1.5	2	3	4	5	6	7

Table 1. Conditions tested with combined high-speed and acoustic measurements.

Incipient Cavitation Events in a Nuclei Deplete Flow

Inception in deplete flows involves intermittent activation of nuclei with subsequent growth of discrete vortical cavities with simultaneous downstream transport.

A typical topology and acoustic signature of an incipient event at a high cavitation number ($\sigma = 6$, $\alpha = 6^\circ$) is presented in figure . A selection of three extracted frames from the high-speed imaging outlines the development of the cavity. The accompanying time series of the acoustic signal, with a 1 kHz high-pass filter applied, is plotted below. The time corresponding to each image is annotated.

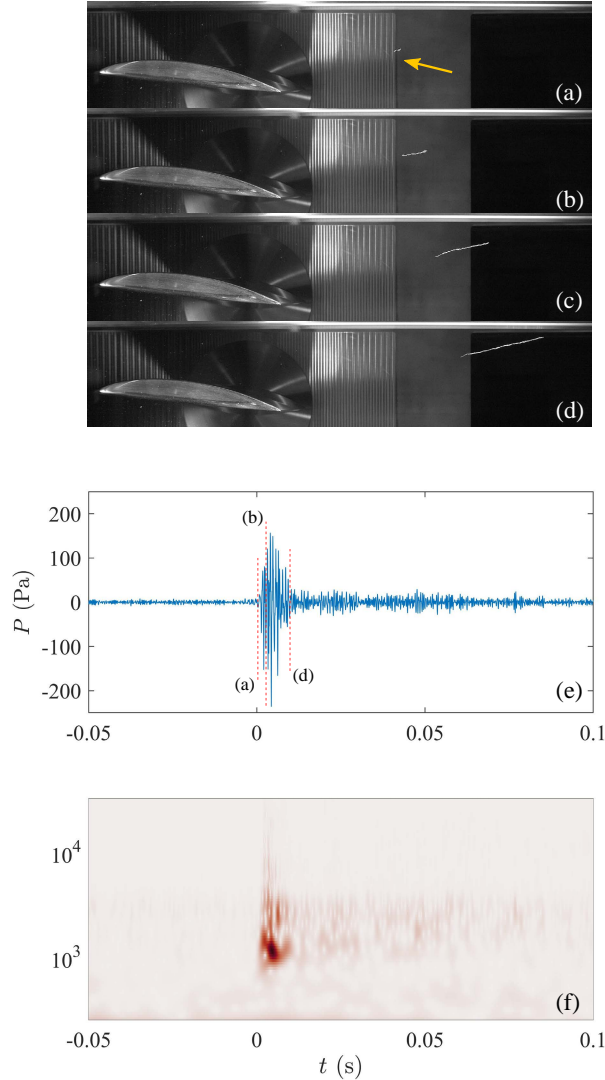


Figure 13. A sequence of images for a typical inception event in a deplete flow, with companion acoustic time series and wavelet transform at $Re = 3 \times 10^6$, $\sigma = 6$, $\alpha = 6^\circ$, $\tau = 0.8$. The wavelet transform is performed for the raw signal, while the time series has been high-pass filtered beyond 1 kHz.

To resolve the frequencies emitted during inception, a wavelet transform of the unfiltered time series is analysed and presented in figure 13e. It should be noted that the tunnel is a confined environment, and that the frequencies present in the acoustic signature may be affected by reverberation. Prior to an isolated nuclei activation event, the time series contained very little acoustic energy. During the growth phase of the cavity, a peak in the wavelet is observed at $f = 1.5$ kHz. Without sudden collapse of the cavity or any significant cavity breakup, the noise emitted during the inception is relatively low, with the acoustic pressure of the order of 100 Pa. Following the initial growth ongoing acoustic emissions remain presumably due to surface modulations evident in the high-speed imaging. This signature persists for a period of the order of 0.1 to 1 ms as the cavity is washed downstream by the flow. The oscillation and migration of the cavity downstream is associated with an increase in wavelet power in the range $1 \text{ kHz} \leq f \leq 5 \text{ kHz}$

An identical analysis, was repeated for the same flow conditions, but at $\sigma = 2.5$, with the results presented in figure 14. At this σ , the decrease in the mean pressure in the core of the TLV, renders a larger proportion of the nuclei contained within the natural population susceptible to inception. Consequently, while the incipient events are still intermittent, there is almost a permanent overlap between the desinence of one event and the inception of a subsequent events.

An incipient event grows rapidly along the TLV and merges with the previous cavity downstream. The acoustic signature during the growth phase resembles that at the higher σ , in terms of both amplitude and frequency. However, as the growing cavity impinges on the leading edge of the previous one, it triggers a momentary collapse at the location of the connection. The condensation shock wave emitted during the cavity collapse is characterized by a spike in the acoustic pressure with an order of magnitude higher amplitude than that of any other noise sources (~ 2000 Pa compared to ~ 100 Pa in figure). This is followed by a period of elevated acoustic signature associated with rebound and oscillation along the cavity. As the effect of merging decays the acoustic signature returns to a

level characteristic of the continuous TLV cavitation.

Overall sound pressure level (SPL) for flow with the natural nuclei population, calculated from a 60 s acoustic recording, is plotted in figure 15 for a range of σ and τ . Generally the SPL increases with decreasing σ for all but the lowest $\sigma = 1.5$ value tested. At this σ value the TLV cavity was now ever-present. The close proximity of the cavity leading edge limits the growth of activated nuclei before merging with the main cavity. The small scale of new cavities results in the less severe collapse events during cavity merging and hence a lower acoustic signature. The SPL also generally increases with decreasing τ reaching a maximum for a particular value depending on σ . Beyond the maximum SPL drops dramatically as the leakage flow within the gap is suppressed. For incipient cavitation at about $\sigma = 0.7$ the maximum SPL occurs for $\tau \approx 0.8$ suggesting a critical condition. Overall these peak occur between $0.4 \leq \tau \leq 1$.

From high-speed imaging it can be observed that the TLV follows a more consistent trajectory, with the cavity assuming a more transparent appearance for $\tau > 1$ (figures 12 and 16). TLV perturbations can be seen to reduce with increasing τ due to reduced confinement combined with diminishing influence of the wall boundary layer turbulence. These effects contribute to the reduction in the SPL with an increase in τ for $\tau \geq 0.8$.

From figure 15 it can be seen that for $\tau = 0.8$ cavitation persists even for the highest cavitation number tested, $\sigma = 7$. Due the mechanical limitations of the facility, a condition free of inception events could not be attained at this Reynolds number and incidence. Persistence of cavitation at lower, yet still relatively high, cavitation numbers was observed across a range of τ .

High-pass filtered acoustic data was also analysed to measure the acoustic event rate by detecting the peaks in the time series. To obtain the event rate, acoustic data was first band-pass filtered ($f_{pass} = 1 - 10$ kHz) and then interrogated to find the locations where the pressure increase between the subsequent points was above the threshold value of 50 Pa. This can happen multiple times

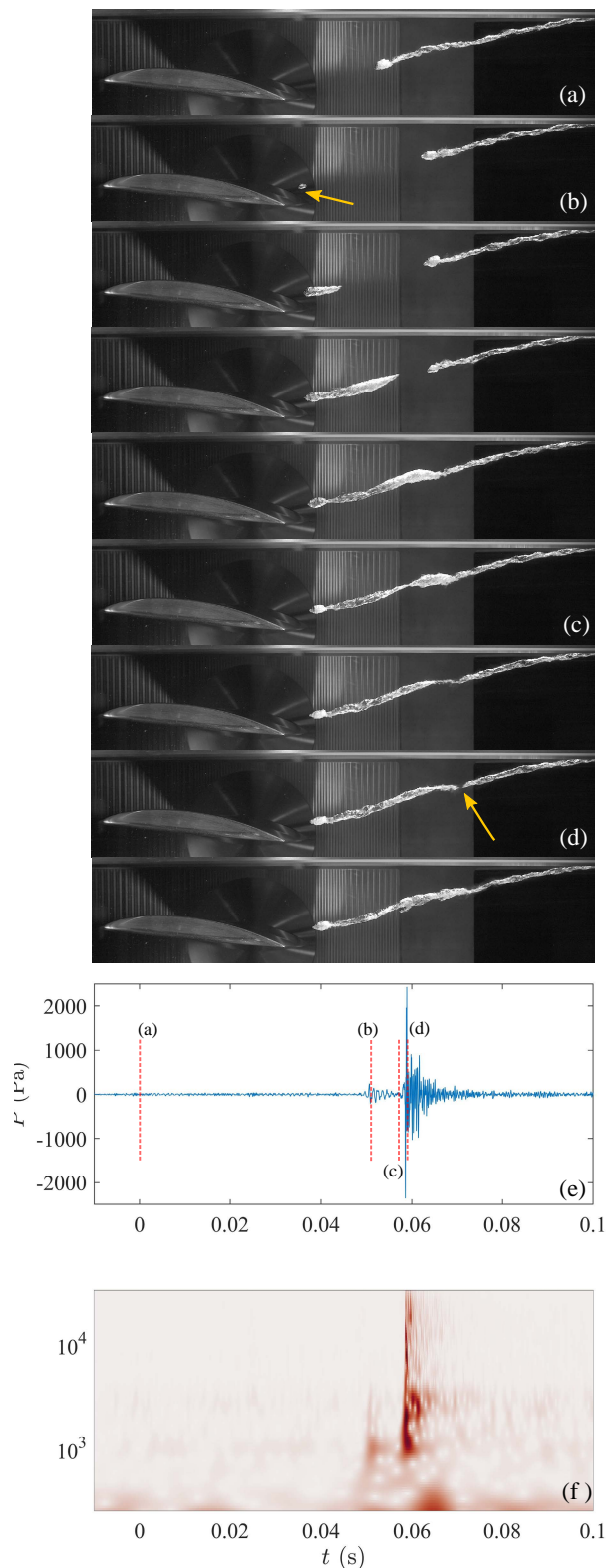


Figure 14. A sequence of images for a typical inception event, with companion acoustic time series and wavelet transform at $Re = 3 \times 10^6$, $\sigma = 2.5$, $\alpha = 6^\circ$, $\tau = 0.8$. The wavelet transform is performed for the raw signal, while the time series has been high pass filtered beyond 1 kHz.

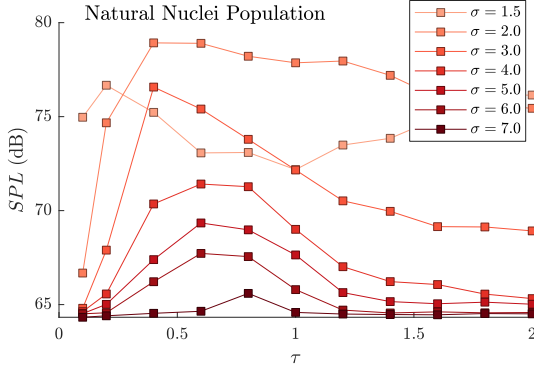


Figure 15. Overall sound pressure level for unseeded flow for a range of σ , and τ at $\alpha = 6^\circ$, and $Re = 3 \times 10^6$.

during a single event so only the events more than 10 ms apart were counted. This event rate may give a higher value than the nuclei activation rate, as there were other events which produced pulses in the acoustic signature, as discussed earlier.

The acoustic event rate across the investigated range of τ and σ are presented in figure 17. As the overall SPL is dominated by the loud acoustic events, the event rate follows a similar trend to that observed in figure 15. However, from figure 17 it is evident that, although cavitation is quieter in an integral sense, the trend in the event rate remained consistent for $\sigma \leq 2$ for all but the smallest gap. From the observations in the high-speed imaging, this may be attributable to an increase in travelling bubble cavitation within the gap.

From the bottom plot in figure 17 it can be observed that increase in the event rate approximately follows a log-linear trend with a decrease in σ . This can be associated with a larger proportion of the nuclei contained within the natural population — which follows a power law — being activated with the reduction in pressure. The variation in the event rate is approximately three orders of magnitude across the range of tested σ . In addition, it is apparent that the flow behaviour changes for $\tau \leq 0.2$, as these curves show substantial deviation from the observed trend. The change is likely due to the TLV being immersed within the wall boundary layer, which has a thickness equivalent to $\tau = 0.3$.

An overall summary of the presented SPL and activation rate data linked to the respective topology of the TLF is presented in figure 16.

Incipient Cavitation Events in a Nuclei Abundant Flow

To investigate the effect of higher nuclei concentrations on TLF cavitation, measurements were repeated with the flow seeded with the abundant population, as presented in figure 10. This population is characterized by a nuclei concentration of $N_b \approx 10 \text{ mL}^{-1}$. For dense seeding, the TLV is continuously fed with bubbles that accumulate in the vortex core.

The SPL for the seeded flow across the complete range of investigated τ and σ values is presented in figure 18. It can be seen that the variation in SPL for a fixed τ was lower for the seeded flow ($\approx 5 \text{ dB}$) than for the natural nuclei population ($\approx 15 \text{ dB}$). Also, a gradual shift in the location of the peak in SPL towards the lower τ values is seen with a decrease in σ .

A change in the trend of SPL with variation in τ can be observed at $\tau \approx 0.6$. Greater SPL is seen for the cases with a low σ and small τ . This is attributed to increased fragmentation and oscillations of the main cavity volume due to the perturbations induced by proximity of the tip to the ceiling and associated wall boundary layer. Additionally, isolated travelling bubble cavities within the gap contribute to the SPL. For $\sigma \geq 4$, cavitation in the gap does not form for small τ so that greater SPL were observed for higher τ values.

A comparison of cavitation topology and acoustic signature of the TLF for the natural nuclei and seeded flow is presented in figure 19. To enable the comparison, the SPL for a complete range of investigated τ values for $\sigma = \{2, 4, 6\}$ is plotted, along with companion high-pass filtered time series segments and representative images of the cavitation topology extracted from high-speed imaging for $\tau = 0.8$.

The comparison of SPL between the natural and abundant nuclei population highlights the complexity that the variation in the nuclei content adds to the flow. For high σ , an increase in the freestream nuclei content is accompanied by a rise in SPL. In contrast, for low σ the SPL is greater for the flow with natural nuclei population. These differences

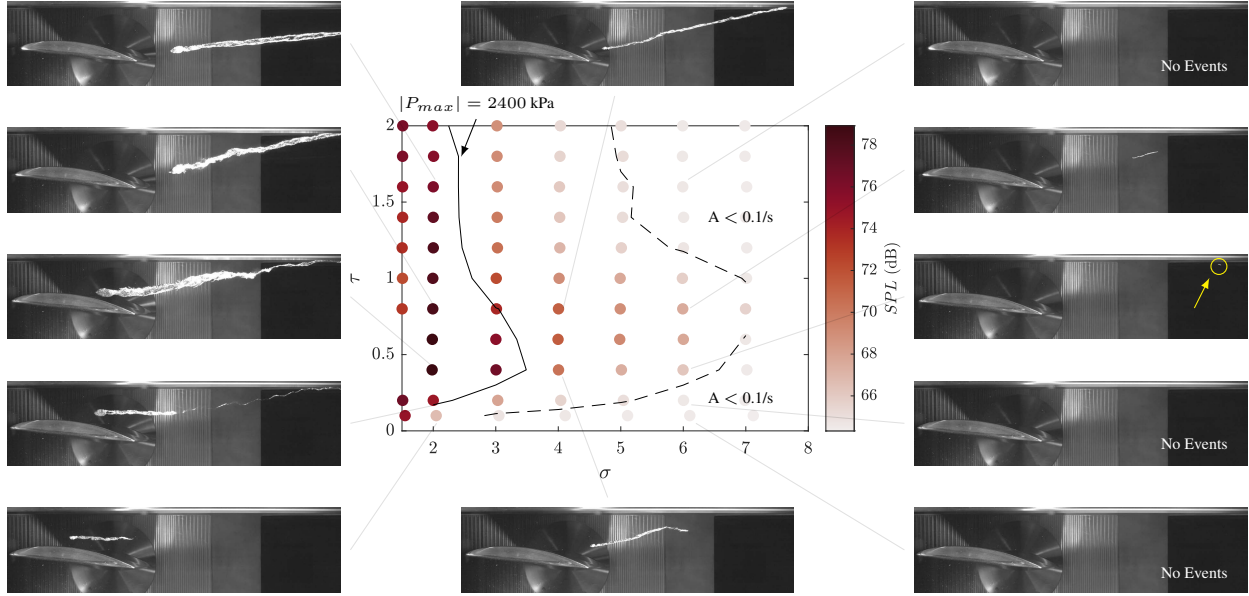


Figure 16. A summary of cavitation topology and inception in tip leakage for the natural nuclei population. The coloured points indicate the overall sound pressure level. The solid contour indicates a maximum acoustic pressure of 2400 Pa. The dashed contour line indicates an activation rate of 0.1 /s.

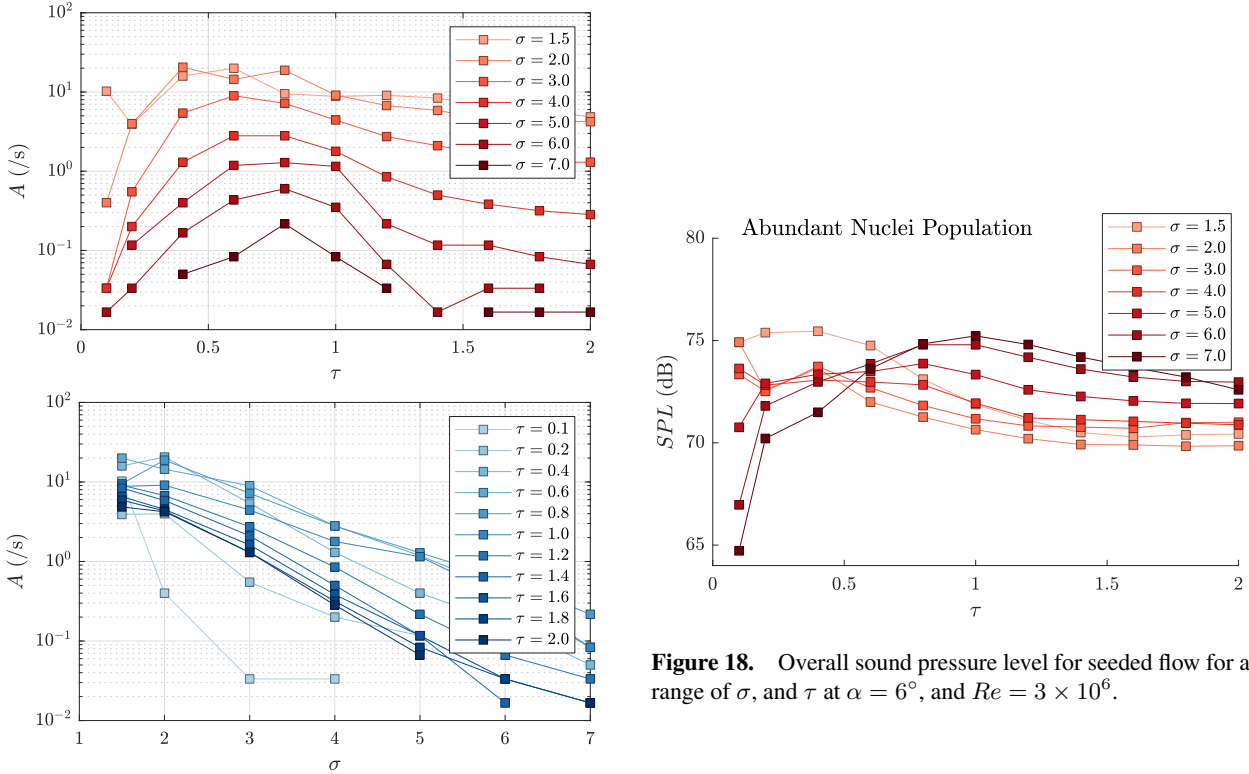


Figure 17. Acoustic cavitation event rate for unseeded flow for a range of σ and τ at $\alpha = 6^\circ$, and $Re = 3 \times 10^6$. The same data are presented in both plots with a different variable on the x-axis.

Figure 18. Overall sound pressure level for seeded flow for a range of σ , and τ at $\alpha = 6^\circ$, and $Re = 3 \times 10^6$.

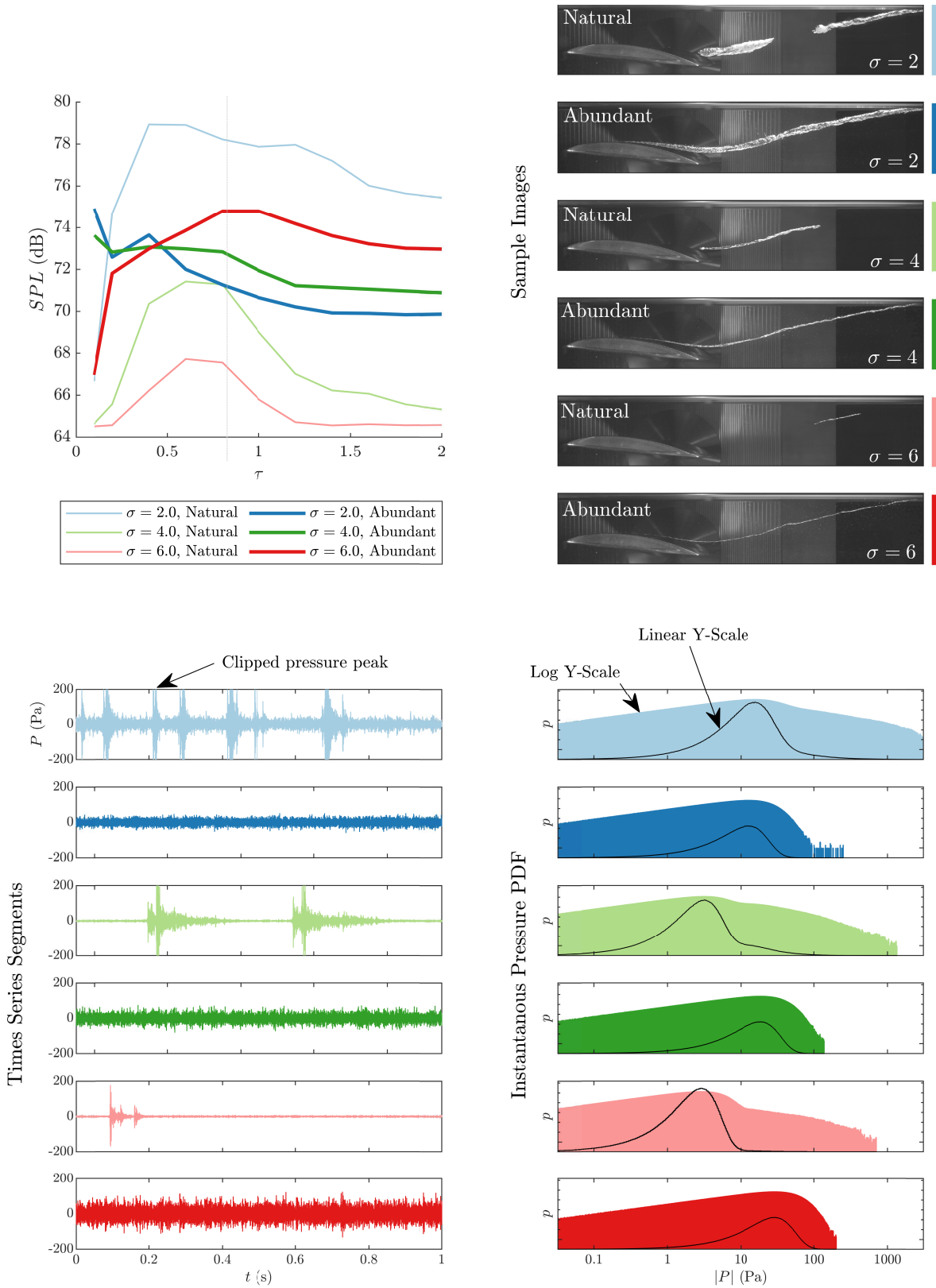


Figure 19. A comparison of overall sound pressure level for both the natural and abundant nuclei populations at $\alpha = 6^\circ$ for varying τ and σ . The time series and histograms and are presented for $\tau = 0.8$, and match the representative images of the flow (top right).

can be explained by analysing the respective time series of the acoustic data.

At $\sigma = 2$ the extremely loud collapse events (from an incipient cavity merging with the downstream cavity) occur often in the natural nuclei flow, while the seeded flow is characterized by a consistent but relatively inactive leakage vortex cavity. The scale and regularity of instantaneous pressures observed in these data are expressed as a probability density function of the absolute value of the high-pass filtered pressure amplitude. These have been plotted with a logarithmic probability scale for the coloured data to ensure that rare loud events are still visible. A linear probability scale for the same data has been superimposed with a black line so that mean pressures can be easily interpreted. These plots show that on average, the natural nuclei and seeded flows have similar instantaneous pressure values for $\sigma = 2$, but it is the acoustic magnitude of the merge/collapse events that increases the overall SPL.

As σ increases, the loud collapse events become less frequent and the SPL of the seeded flow surpasses that of the flow with the natural nuclei. This can be attributed to an elevated baseline SPL associated with the presence of a continuous TLV cavity in seeded flow, in comparison to the lower baseline SPL during the periods without cavitation in the natural nuclei flow. Additionally, a slight increase in the baseline SPL with a decrease in σ is noticeable for the seeded flow. This can be attributed to a lesser opportunity for growth of the activated nuclei before joining the main cavity, due to a shift of the main cavity leading edge closer to the hydrofoil with a decrease in σ .

In summary for the natural flow noise levels are controlled by the event rate of nuclei activations and the much louder vortex cavity merging events. Both the intensity and rate of these increase with decreasing cavitation number and reach a peak for a particular tip gap. For the seeded flow, noise levels are controlled by continuous sources presumably due to local dynamic behaviour of the globally stable vortex cavity. There is a clear cross over between the combined effect of σ , bubble concentration and size which is modulated by the gap height. Further testing is needed to explore how this

change transitions for intermediate nuclei populations. There is however, a critical gap height ratio with poor cavitation performance, but this value may change with the available freestream nuclei population.

Conclusion

A newly designed hydrofoil model with a complex tip fairing proved successful in addressing the issues observed in previous studies of cavitation in the TLF at the AMC. A traversing system capable of continuous indexation of the gap clearance (τ) and hydrofoil incidence α enables efficient conduct of the experiment. The effect of nucleation was investigated by performing the experiments for two freestream nuclei populations, a sparse natural nuclei population and a population abundantly seeded with larger nuclei.

The topology of the developed cavitation was characterized for a wide range of τ and α values. For large τ and small α cavitation was observed in the TLV and resembled TVC characteristic of an unbounded flow around a three-dimensional hydrofoil. With an increase in α , cavitation topology became more complex, with secondary vortical structures originating from the tip trailing edge and jetting shear layer on the suction side of the hydrofoil interacting with the TLV. For high α and small τ travelling bubble and attached cavitation was observed within the gap. Generally, the cavitation in natural nuclei flow was observed to have an intermittent character, becoming more continuous with the introduction of seeding.

Based on the observations of the cavity topology, an incidence of $\alpha = 6^\circ$ was chosen for further characterization using acoustic measurements. From these, a critical gap clearance with the highest incipient cavitation number in the natural nuclei flow was found for $\tau = 0.8$. For the seeded flow, cavitation was persistent at the highest cavitation numbers (σ) achievable in the experimental facility, and inception was not fully resolved.

Acoustic measurements reveal a higher baseline acoustic signature for the seeded flow, stemming from the presence of a continuous cavity.

The intermittent character of cavitation for the natural nuclei flow gives a lower baseline noise, however, inception and in particular collapse associated with merging between successive cavitation events was observed as a flow feature with the highest instantaneous peaks in acoustic pressure.

The observation of cavitation in secondary vortical structures indicates the flow topology for the current stationary hydrofoil analogy is approaching that observed in the multi-bladed rotating machinery. Further work on characterizing inception for conditions where secondary vortical structures were observed is planned.

The influence of nucleation was examined for the two extremes of nuclei populations in which turbomachinery and ducted propulsors typically operate, and such an approach highlights the significant effects the nuclei population have on cavitation in the TLF. Future efforts will concentrate on characterization of cavitation inception and dynamics across a range of intermediate poly-, and monodisperse nuclei populations.

References

- Abbott, I.H. & von Doenhoff, A.E. 1959 *Theory of Wing Sections (Including a summary of airfoil data)*, dover edition edn. New York: Dover Publications, Inc.
- Agarwal, K., Ram, O., Wang, J., Lu, Y. & Katz, J. 2020 Measuring the 3D pressure field and relating it to cavitation inception in a turbulent shear layer. In *33rd Symposium on Naval Hydrodynamics*.
- Arndt, R. E. A. & Maines, B. H. 1994 Viscous effects in tip vortex cavitation and nucleation. In *20th Symposium on Naval Hydrodynamics*.
- Barbaca, L., Russell, P. S., Pearce, B. W. & Brandner, P. A. 2020a Characterization of microbubble generation in a confined turbulent jet. In *Proceedings of the 22nd Australasian Fluid Mechanics Conference*.
- Barbaca, L., Venning, J. A., Russell, P. S., Russell, E. S. C., Pearce, B. W. & Brandner, P. A. 2020b Dynamics of cavitation inception in high Reynolds number shear flow. In *Proceedings of the 33rd Symposium on Naval Hydrodynamics*.
- Boulon, O., Callenaere, M., Franc, J. & Michel, J. 1999 An experimental insight into the effect of confinement on tip vortex cavitation of an elliptical hydrofoil. *Journal of Fluid Mechanics* **390**, 1–23.
- Boulon, O., Franc, J. & Michel, J. 1997 Tip vortex cavitation on an oscillating hydrofoil. *Journal of Fluids Engineering* **119** (4), 752–758.
- Brandner, P. A., Lecoffre, Y. & Walker, G. J. 2006 Development of an Australian national facility for cavitation research. In *Sixth International Symposium on Cavitation - CAV 2006*.
- Brandner, P. A., Lecoffre, Y. & Walker, G. J. 2007 Design considerations in the development of a modern cavitation tunnel. In *Proceedings of the 16th Australasian Fluid Mechanics Conference, 16AFMC*, pp. 630–637.
- Breslin, John P. & Andersen, Poul 1994 *Hydrodynamics of Ship Propellers*. Cambridge: Cambridge University Press.
- Briancon-Marjollet, L. & Merle, L. 1996 Inception, development and noise of a tip vortex cavitation. In *21st Symposium on Naval Hydrodynamics*.
- Carlton, John 2007 *Marine Propellers & Propulsion*, 2nd edn. Oxford: Butterworth-Heinemann.
- Chang, N. A., Choi, J., Yakushiji, R. & Ceccio, S. L. 2012 Cavitation inception during the interaction of a pair of counter-rotating vortices. *Physics of Fluids* **24** (1), 014107.
- Cheng, H., Ji, B., Long, X., Huai, W. & Farhat, M. 2021 A review of cavitation in tip-leakage flow and its control. *Journal of Hydrodynamics* **33** (2), 226–242.
- Doolan, C., Brandner, P., Butler, D., Pearce, B., Moreau, D. & Brooks, L. 2013 Hydroacoustic characterization of the AMC cavitation tunnel. In *In Acoustic 2013, Victor Harbour, Australia*.
- Drela, M. 1989 *XFOIL: An analysis and design system for low Reynolds number airfoils*. Notre Dame, Indiana, USA: Springer-Verlag.

- Dreyer, M. 2015 Mind the gap: Tip leakage vortex dynamics and cavitation in axial turbines. PhD Thesis.
- Gopalan, S., Katz, J. & Knio, O. 1999 The flow structure in the near field of jets and its effect on cavitation inception. *Journal of Fluid Mechanics* **398**, 1–43.
- Gopalan, S., Katz, J. & Liu, H. L. 2002 Effect of gap size on tip leakage cavitation inception, associated noise and flow structure. *Journal of Fluids Engineering* **124** (4), 994–1004.
- de Graaf, K.L., Pearce, B. W. & Brandner, P. A. 2016 The influence of nucleation on cloud cavitation about a sphere. In *16th International Symposium on Transport Phenomena and Dynamics of Rotating Machinery (ISROMAC16)*.
- Guo, Q., Zhou, L. & Wang, Z. 2016 Numerical evaluation of the clearance geometries effect on the flow field and performance of a hydrofoil. *Renewable Energy* **99**, 390–397.
- Higashi, S., Yoshida, Y. & Tsujimoto, Y. 2002 Tip leakage vortex cavitation from the tip clearance of a single hydrofoil. *JSME International Journal Series B Fluids and Thermal Engineering* **45** (3), 662–671.
- Kerwin, Justin E. & Hadler, Jacques B. 2010 *The Principles of Naval Architecture Series. Propulsion*. Jersey City, New Jersey: SNAME.
- Khoo, M. T., Venning, J. A., Pearce, B. W. & Brandner, P. A. 2021 Nucleation and cavitation number effects on tip vortex cavitation dynamics and noise. *Experiments in Fluids* **62** (10), 1–19.
- Khoo, M. T., Venning, J. A., Pearce, B. W., Takahashi, K., Mori, T. & Brandner, P. A. 2020 Natural nuclei population dynamics in cavitation tunnels. *Experiments in Fluids* **61** (2), 34.
- Laborde, R., Chantrel, P. & Mory, M. 1997 Tip clearance and tip vortex cavitation in an axial flow pump. *Journal of Fluids Engineering* **119** (3), 680–685.
- O’Hern, T. J. 1990 An experimental investigation of turbulent shear flow cavitation. *Journal of Fluid Mechanics* **215**, 365–391.
- Oweis, G. F. & Ceccio, S. L. 2005 Instantaneous and time-averaged flow fields of multiple vortices in the tip region of a ducted propulsor. *Experiments in Fluids* **38** (5), 615–636.
- Peng, X., Xu, L. & Cao, Y. 2017 The study of tip vortex flow and cavitation inception on an elliptical hydrofoil. In *5th International Symposium on Marine Propulsion*.
- Ran, B. & Katz, J. 1994 Pressure fluctuations and their effect on cavitation inception within water jets. *Journal of Fluid Mechanics* **262**, 223–263.
- Russell, P. S., Barbaca, L., A., Venning, J., Russell, E. S. C., Pearce, B. W. & Brandner, P. A. 2020a Cavitation in tip-leakage flows. In *33rd Symposium on Naval Hydrodynamics*.
- Russell, P. S., Barbaca, L., Venning, J. A., Pearce, B. W. & Brandner, P. A. 2020b Measurement of nuclei seeding in hydrodynamic test facilities. *Experiments in Fluids* **61** (3), 79.
- Russell, P. S., Barbaca, L., Venning, J. A., Pearce, B. W. & Brandner, P. A. 2020c Nucleation effects on tip-gap cavitation. In *22nd Australasian Fluid Mechanics Conference (AFMC2020)*, pp. 1–4.
- Venning, J. A., Smith, S., Brandner, P. A., Giosio, D. & Pearce, B. W. 2017 The influence of nuclei content on cloud cavitation about a hydrofoil. In *17th International Symposium on Transport Phenomena and Dynamics of Rotating Machinery (ISROMAC17)*.
- Wu, H., Tan, D., Miorini, R. L. & Katz, J. 2011 Three-dimensional flow structures and associated turbulence in the tip region of a waterjet pump rotor blade. *Experiments in Fluids* **51** (6), 1721–1737.
- You, D., Wang, M., Moin, P. & Mittal, R. 2006 Effects of tip-gap size on the tip-leakage flow in a turbomachinery cascade. *Physics of Fluids* **18** (10), 105102.
- You, D., Wang, M., Moin, P. & Mittal, R. 2007 Vortex dynamics and low-pressure fluctuations in the tip-clearance flow. *Journal of Fluids Engineering* **129** (8), 1002–1014.

Zhang, D., Shi, W., van Esch, B., Shi, L. & Dubuisson, M. 2015 Numerical and experimental investigation of tip leakage vortex trajectory and dynamics in an axial flow pump. *Computers & Fluids* **112**, 61–71.